Research Article Vol. 9, No. 11 | 1 Nov 2018 | BIOMEDICAL OPTICS EXPRESS 5678

Biomedical Optics EXPRESS

Depth-multiplexed optical coherence tomography dual-beam manually-actuated distortion-corrected imaging (DMDI) with a micromotor catheter

ANTHONY M. D. LEE,* CALUM MACAULAY, AND PIERRE LANE

Imaging Unit, Department of Integrative Oncology, British Columbia Cancer Research Centre, Vancouver, BC V5Z 1L3, Canada
**alee@bccrc.ca*

Abstract: We present a new micromotor catheter implementation of dual-beam manually-actuated distortion-corrected imaging (DMDI). The new catheter called a depth-multiplexed dual-beam micromotor catheter, or mDBMC, maintains the primary advantage of unlimited field-of-view distortion-corrected imaging along the catheter axis. The mDBMC uses a polarization beam splitter and cube mirror to create two beams that scan circularly with approximately constant separation at the catheter surface. This arrangement also multiplexes both imaging channels into a single optical coherence tomography channel by offsetting them in depth, requiring half the data bandwidth compared to previous DMDI demonstrations that used two parallel image acquisition systems. Furthermore, the relatively simple scanning pattern of the two beams enables a straightforward automated distortion correction algorithm. We demonstrate the imaging capabilities of this catheter with a printed paper phantom and in a section of dragon fruit.

© 2018 Optical Society of America under the terms of the OSA Open Access Publishing Agreement

1. Introduction

Numerous fiber optic two-dimensional scanning catheters have been developed for endoscopic optical imaging [1,2]. Side-looking rotary-pullback catheters using proximal or distal rotary motors are ideal for examining luminal organs and several research groups have demonstrated exquisite imaging in fields such as cardiology [3,4], gastroenterology [5–7], and respirology [8,9]. However, rotary-pullback catheters require that there is no relative motion between the subject and catheter sheath to provide high-fidelity imaging, a constraint that may be difficult to achieve in clinical settings. A further limitation of rotary-pullback catheters is that their field-of-view (FOV) along the catheter axis is limited by the stroke of the pullback actuator. Acquiring a larger FOV requires resetting and repositioning of the catheter and image stitching. Extension of FOV has been realized using side-looking rotary imaging capsules that are manually actuated along the fiber axis [10,11] but this comes at the expense of image distortions along the manually actuated dimension due to non-constant actuation velocity. Manual actuation image distortions can be corrected by combining the imaging devices with additional sensors such as camera [12], encoder [13], magnetic [14], or optical [15] tracking. However, these techniques add additional hardware complexity, may not be practical for endoscopic catheters, and can introduce new challenges such as keeping the imaging environment clear of magnetic field altering materials in the case of magnetic tracking.

We previously demonstrated a two-dimensional scanning technique called dual-beam manually-actuated distortion-corrected imaging (DMDI) that addresses the limited-FOV and subject/catheter sheath motion distortion limitations of the aforementioned two-dimensional scanning techniques [16,17]. A DMDI scanner collects two images using a single-axis mechanical actuator to scan two beams across a sample primarily along one dimension while simultaneously manually actuating the scanner along the orthogonal direction. By knowing the

#341581 https://doi.org/10.1364/BOE.9.005678
Journal © 2018 Received 22 Aug 2018; revised 3 Oct 2018; accepted 3 Oct 2018; published 23 Oct 2018

Biomedical Optics EXPRESS

distance between the beams and the time difference between when one beam passes a feature also imaged by the second beam, the scanner velocity can be estimated and subsequently used to correct image distortions due to manual actuation and/or subject motion.

We first implemented DMDI in a dual-beam micromotor catheter (DBMC) with the primary advantages being simplified scanner design, the ability to capture unlimited field-of-view along the catheter axis, and the ability to correct for relative subject-catheter sheath motion during imaging [16]. However, the original DBMC has some severe limitations, namely a complex beam scanning pattern that requires laborious manual image co-registration for velocity estimation, and the need for duplicate image acquisition hardware that also correspondingly doubles the data bandwidth.

We subsequently demonstrated a galvanometer-based implementation of DMDI [17] that scans two parallel imaging beams across a sample. Using this beam scanning pattern, we were able to develop a straightforward algorithm based on cross correlation of line images, or frames, to automate feature co-registration between the two images. This enables rapid image distortion correction and greatly improves the clinical potential of DMDI.

In this work, we present a new optical coherence tomography (OCT) DMDI catheter, called a multiplexed dual beam micromotor catheter, or mDBMC, that uses a polarization beam splitter/cube mirror combination attached to a micromotor to scan two almost-parallel beams on the catheter outer diameter. This simplified scan pattern enables the use of an automated distortion correction algorithm analogous to that developed for the galvanometer scanner. Additionally, the mDBMC multiplexes the two imaging channels into a single OCT data acquisition channel by offsetting them in the depth dimension, reducing data bandwidth requirements by a factor of two compared to previous DMDI implementations. We demonstrate DMDI with the mDBMC by imaging a printed paper phantom and a section of dragon fruit.

2. Distortion correction algorithm

A DBMC uses a pair of beams (denoted A and B) that are scanned rotationally with a micromotor while manually actuating the catheter or the sample along the catheter axial axis (z axis). Rotational actuation around the catheter azimuthal axis (θ axis) is also permitted. While actuating, $A(N)$ and $B(N)$, a pair of one-dimensional image streams are collected as a function of time index $N(t) = f_{pixel} \times t$, where f_{pixel} is the pixel clock frequency (For notational simplicity, the time dependence of $N(t)$ will be omitted onwards).

The scan paths of the A and B beams on the DBMC outer surface can be complex. A one-time calibration with a calibration phantom is needed to determine the path of the A and B beams as a function of time. The azimuthal positions of the A and B beams at the catheter surface as a function of time can be determined and are represented by the functions $\theta_A(n_A)$ and $\theta_B(n_B)$, respectively, which are periodic in N_{fr}, the number of image points per micromotor rotation. These angular calibration functions are referenced relative to a common optical marker that is imaged at $N_{ref,(A,B)}$, such that $n_{(A,B)} = N\text{-}N_{ref,(A,B)}$ is the intraframe pixel index. (Note: Here we use the subscripted (A,B) to represent two distinct terms or functions corresponding to each of the A and B imaging channels.) These functions allow remapping and resampling of the $A(N)$ and $B(N)$ image streams to two-dimensional $A(fr_A,\theta)$ and $B(fr_B,\theta)$ images, where $fr_{(A,B)}$, the line indices (or frame indices if using a three-dimensional imaging modality like optical coherence tomography [OCT]), are the integer division of $n_{(A,B)}$ by N_{fr}. The axial scan positions of the beams are calibrated and can be fit to a pair of functions called the scan pattern function $S(\theta)$ and the fixed pattern function $F(\theta)$. $S(\theta)$ is twice the separation of the beams along the z axis and allows estimation of the catheter velocity. $F(\theta)$ is the z difference between the path of the midpoint of the two beams and a perfect circle allowing correction of non-circular scan patterns.

For sample imaging, a single image feature j, co-registered in both images at points $(fr_{A,j},\theta_{A,j})$ and $(fr_{B,j},\theta_{B,j})$, corresponding to time-angle coordinates $(t_{A,j},\theta_{A,j})$ and $(t_{B,j},\theta_{B,j})$ respectively, can be used to estimate the average axial, $\overline{v}_{z,j}$, and azimuthal $\overline{\omega}_j$ velocities in the time interval between $t_{A,j}$ and $t_{B,j}$ as:

Biomedical Optics EXPRESS

$$\bar{v}_{z,j} = \frac{S(\theta_{A,j}) + S(\theta_{B,j})}{t_{B,j} - t_{A,j}} \tag{1}$$

$$\bar{\omega}_j = \frac{\theta_{B,j} - \theta_{A,j}}{t_{B,j} - t_{A,j}} \tag{2}$$

After co-registering multiple image features between the A and B images, the instantaneous velocities as a function of time can be calculated by taking weighted averages of all interval velocities defined at that time:

$$v_z(t) = \frac{\sum_j \left(\bar{v}_{z,j} \cdot w_j(t)\right)}{\sum_j w_j(t)} \tag{3}$$

$$\omega(t) = \frac{\sum_j \left(\bar{\omega}_j \cdot w_j(t)\right)}{\sum_j w_j(t)} \tag{4}$$

where $w_j(t)$ is the normalized weighting function:

$$w_j(t) = \begin{cases} \dfrac{1}{\left|t_{B,j} - t_{A,j}\right| + 1}, & t \in [t_{B,j}, t_{A,j}] \\ 0, & elsewhere \end{cases} \tag{5}$$

The instantaneous velocities can be integrated to calculate the catheter axial and azimuthal displacements, $z_{cath}(t)$ and $\varphi_{cath}(t)$ respectively. Using these displacements, the $A(N)$ and $B(N)$ images can be distortion corrected by remapping them to $A(Z_A,\Theta_A)$ and $B(Z_B,\Theta_B)$ where

$$Z_A(t,\theta_A) = z_{cath}(t) - S(\theta_A) - F(\theta_A) \tag{6}$$

$$Z_B(t,\theta_B) = z_{cath}(t) + S(\theta_B) - F(\theta_B) \tag{7}$$

$$\Theta_A(t) = \theta_A(t) - \varphi_{cath}(t) \tag{8}$$

$$\Theta_B(t) = \theta_B(t) - \varphi_{cath}(t) \tag{9}$$

3. Methods

3.1 OCT imaging system

The OCT imaging system uses a 23 mW, f_{laser} = 100 kHz, 1310 nm swept-source laser (AXP50125-6, Axsun Technologies, Billerica, MA) that feeds a standard Mach-Zehnder OCT interferometer. The sample arm of the interferometer is connected to the catheter pigtail. A balanced detector (PDB480-AC, Thorlabs Inc., Newton, NJ) is digitized by a k-clocked acquisition board (ATS9350, Alazar Technologies, Inc., Point Claire, QC) controlled by in-house developed data acquisition software.

3.2 OCT multiplexed dual beam micromotor catheter

The OCT multiplexed dual beam micromotor catheter (mDBMC) used for these experiments is shown in Fig. 1(i-iii). To create a cube mirror, a pair of aluminum-coated 1.5 mm right angle prisms (MPCH-1.5, Tower Optical Corporation, Boynton Beach, FL) were mounted with UV-curing adhesive hypotenuse-to-hypotenuse and to the shaft of a 4 mm OD micromotor (SBL04-0829, Namiki Precision of California, Inc., Belmont, CA) at an angle of approximately 8° to avoid back-reflections into the imaging system. A 1310 nm antireflection-coated 1.5 mm cube

Biomedical Optics EXPRESS

polarization beam splitter (PBS, FOCtek Photonics, Inc., Fuzhou, China) was mounted to the cube mirror with the beam splitting face oriented parallel to the reflective face of the cube mirror as shown in Fig. 1(i-iii).

A dual SMF-28 fiber pigtail (DFP, KFP-V-2-8D-250S-250-1310-FC/APC, Photop Technologies, Inc., Santa Clara, CA) was aligned to a GRIN lens (GRIN2313A, Thorlabs Inc., Newton, NJ) inside a glass ferrule (51-2800-1800, Thorlabs, Inc.). Both the DFP and entrance face of the GRIN lens were polished at 8° and the faces of the DFP and GRIN were anti-reflection coated for 1310 nm. The fibers within the DFP are separated by 250 μm and oriented vertically to one another if viewing the 8° polish angle from the side. Although only a single fiber is used for imaging, a DFP was used rather than the corresponding on-axis single fiber pigtail to obtain better beam optics. As shown in Fig. 1(ii), the chief ray of the upper fiber of the DFP refracts at the 8° surfaces and travels approximately collinear along the GRIN axis. An analogous beam from an on-axis single fiber pigtail would refract away from the GRIN axis and also emerge at an angle to the exit face. The distance between the DFP and GRIN was adjusted and fixed with UV-curing adhesive (NOA 63, Norland Products Inc., Cranbury, NJ) to place the focus of a 1310 nm light source approximately 4.8 mm from the end face of the GRIN with a circular spot size of 14 μm FWHM measured with a beam profiler (BeamMap2, DataRay Inc., Redding, CA).

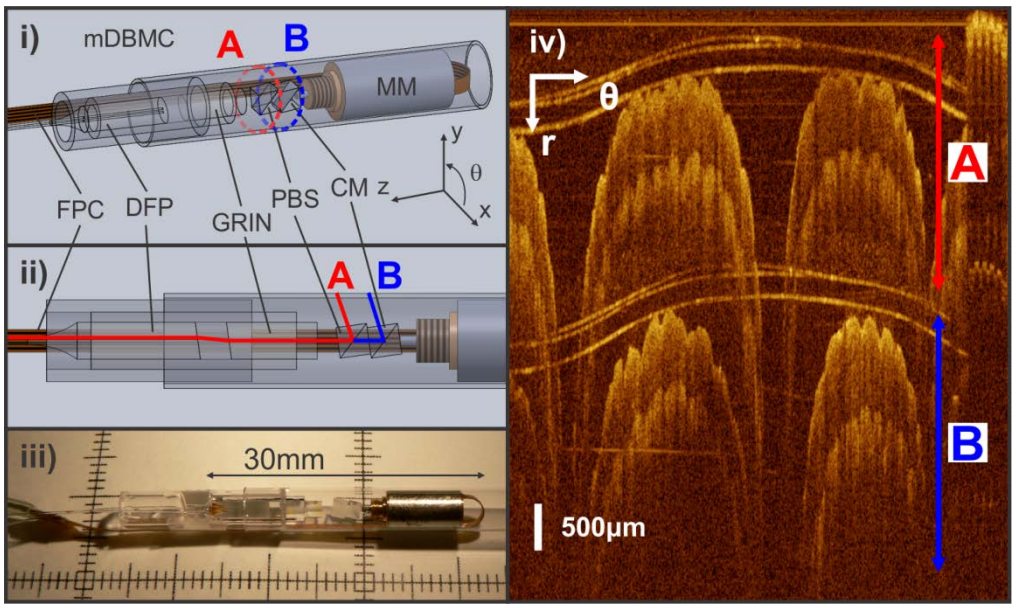

Fig. 1. OCT multiplexed dual-beam micromotor catheter (mDBMC). i) Model view of the mDBMC. The approximate scan patterns of the A and B beams on the catheter surface are shown as red and blue dashed lines respectively. FPC = flexible printed circuit, DFP = dual fiber pigtail, GRIN = graded-index lens, PBS = polarization beam splitter, CM = cube mirror, MM = 4 mm OD micromotor. ii) Side view of the mDBMC model showing the approximate beam paths of the A (red) and B (blue) beams. iii) Photograph of the mDBMC with the minimum possible rigid length indicated. The smallest divisions of the background scale are 1 mm. iv) OCT image of fingers taken with the mDBMC showing the depth displacement of the A and B imaging channels. The scale bar is for length in air.

The DFP/GRIN subassembly was inserted into a clear plastic tube with the same outer diameter as the micromotor. The flexible printed circuit (FPC) feeding power to the micromotor was bent back alongside the motor and held against it with another length of thin-walled plastic tube to give an overall catheter OD of 4.7 mm. The minimum possible rigid length of the catheter is 30 mm. A commercial driver board (SOD12ST, Namiki Precision of California, Inc.) was used to drive the micromotor at a frame rate of f_{fr} = 100 Hz resulting in N_{fr} = 1000 A-lines

Biomedical Optics EXPRESS

per rotational frame. No frame-to-frame non-uniform rotational distortion (NURD) was observed when using this motor and driver combination.

The light paths for the imaging beams are approximately shown in Fig. 1(ii). Light from the swept source laser is polarized but becomes randomly elliptically polarized traveling through the single mode fiber leading to the mDBMC. The component of light exiting the DFP/GRIN subassembly that is *s*-polarized relative to the PBS hypotenuse surface is reflected from the PBS (A imaging beam) while the *p*-polarized component is transmitted and reflects off the cube mirror hypotenuse (B imaging beam). At the catheter surface, the two beams maintain approximately constant separation along the *z* axis as the micromotor rotates. In the final assembly, the focus of the A beam is located outside of the catheter and that of the B beam is inside the catheter, such that the average working distance of the A and B beams is approximately at the catheter surface. An example image frame of fingers with the mDBMC is shown in Fig. 1(iv). The B image is shifted lower (larger *r*) compared to the A image due to the extra optical path length traveled by the B beam. The FPC is the feature at the rightmost of Fig. 1(iv), and makes an easily identifiable reference feature in the azimuthal dimension.

3.3 mDBMC calibration

The procedure for calibrating the mDBMC is outlined on the left side of Fig. 2. A calibration phantom was printed on standard white printer paper consisting of a pattern of equally spaced vertical and horizontal lines. This pattern was wrapped around a 4.75/5.00 mm ID/OD plastic tube and fixed with tape to yield equally spaced lines along the θ axis and lines 169 μm wide with 169 μm spacing along the *z* axis. The calibration image was acquired first with a stationary pause over the lines along the θ axis and then using a stepper motor to push the mDBMC at a speed of 2 mm/s for 20 mm total length over the equally spaced lines along the *z* axis [Fig. 3(i)]. To generate the $A(N)$ and $B(N)$ image streams, the top 250 pixels in the *r* dimension, corresponding to 1.24 mm in air, below the respective outer sheath contours were averaged. Using the edge of the FPC as the azimuthal reference position, which conveniently coincides for both the A and B beam, the calibration procedure described previously in [16] was used to determine $\theta_A(n_A)$ and $\theta_B(n_B)$, the angular scan patterns, and $S(\theta)$ and $F(\theta)$, the functions determining the axial scan pattern. Briefly, the images were aligned along the edge of the flexible printed circuit cable and pre-processed to remove image shear due to the asynchronous operation of the micromotor and data acquisition system. The portions of the images when the mDBMC was stationary, where the lines of the phantom were equally spaced along the θ direction, were used to fit $\theta_A(n_A)$ and $\theta_B(n_B)$ to functions consisting of a linear component plus a second-order Fourier series. Secondly, the positions of the equally spaced lines along the *z* axis were used to fit $S(\theta)$ and $F(\theta)$ to second-order Fourier series.

3.4 Sample imaging and distortion correction

A printed paper phantom and a dragon fruit were imaged to demonstrate DMDI imaging with the mDBMC. For the paper phantom, a printed QR code was wrapped around a 4.75/5.00 mm ID/OD plastic tube at an angle such that the pixelation axes of the QR code were not aligned to either of the *z* or θ axes. Imaging was collected while pushing the mDBMC through the QR code phantom manually along the *z* dimension while simultaneously oscillating along the θ dimension.

For the dragon fruit, a 4.75/5.00 mm ID/OD plastic tube was inserted through a section of the fruit to remove a core of the white flesh. The plastic tube was left in place and the mDBMC was inserted into it. Imaging was acquired while manually pushing and rotating the mDBMC through the plastic tube.

Biomedical Optics EXPRESS

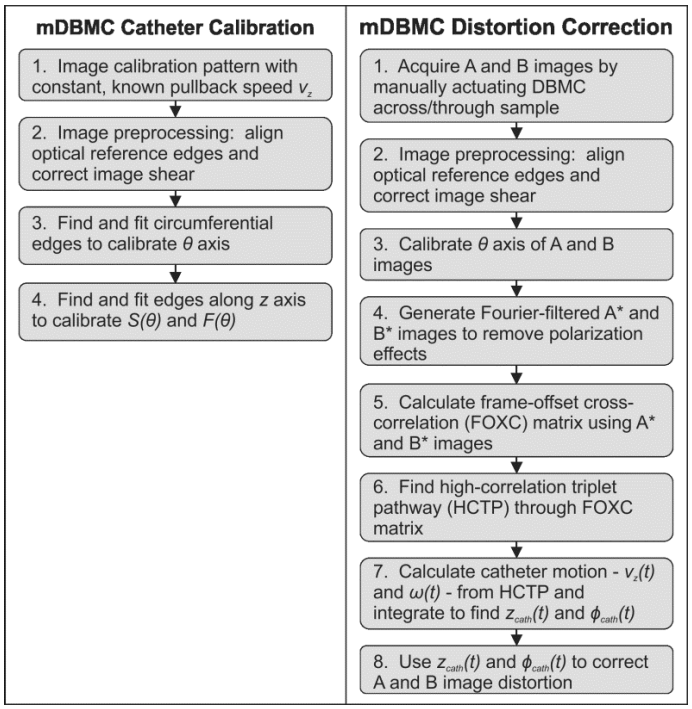

Fig. 2. Outline of the major steps for calibrating and correcting images acquired with the depth-multiplexed dual beam micromotor catheter (mDBMC).

The procedure for performing image distortion correction with the mDBMC is outlined on the right side of Fig. 2. In both cases, the *A(N)* and *B(N)* image streams were aligned and preprocessed as for the calibration phantom. Automated distortion correction of the images was performed using the frame cross correlation method described in [17] with the following modifications. First, the image streams were angle-calibrated and resampled to provide *en face* $A(fr_A,\theta)$ and $B(fr_B,\theta)$ images consisting of 1000 equally-spaced angular pixels. For feature co-registration, secondary $A^*(fr_A,\theta)$ and $B^*(fr_B,\theta)$ images were created to remove slow intensity variations along the θ dimension corresponding to polarization effects by first cropping 95 of the 1000 pixels to remove the image of the FPC, and then Fourier filtering in the θ dimension to remove frequencies lower than 5/905 pixels^{-1}. The Fourier-filtered images were used for determining the frame-offset cross-correlation (FOXC) matrices and the subsequent high correlation triplet pathways (HCTP) as detailed in [17] except with the offset dimension being an angular displacement rather than a linear one. An additional filtering step of the frame-offset triplets was applied for the dragon fruit imaging to remove spurious triplets corresponding to very high and non-realistic angular accelerations. For each triplet j in the HCTP, the average axial and angular velocities between frames fr_A,j and fr_B,j were calculated as

$$\bar{v}_{z,j} = \frac{\bar{S} \times f_{fr}}{fr_{B,j} - fr_{A,j}} \tag{10}$$

$$\bar{\omega}_j = \frac{(\theta_{B,j} - \theta_{A,j}) \times f_{fr}}{fr_{B,j} - fr_{A,j}} \tag{11}$$

where the constant $\bar{S}$ is the average of $S(\theta)$ over all angles. Assuming that any image frame fr is collected in its entirety instantaneously at $t = fr/f_{fr}$, the instantaneous axial and angular velocities $v_z(t)$ and $\omega(t)$ were determined using Eqs. (3)-(5). Integration of the corresponding

Biomedical Optics EXPRESS

velocities yielded the axial and angular displacements that were then used to produce the corrected $A(Z_A,\Theta_A)$ and $B(Z_A,\Theta_A)$ images using Eqs. (6)-(9).

4. Results

4.1 Calibration

The results of the calibration procedure are shown in Fig. 3. The preprocessed $A(n_A,fr_B)$ and $B(n_B,fr_B)$ images [Fig. 3(i)], show the appearance of the calibration lines parallel to the z and θ dimensions as scanned by the two beams of the mDBMC. Common features appear at lower frame indices in the A image compared to the B image as the mDBMC is pushed through the calibration pattern in the + z direction. The similar bent shape of the vertical lines in Fig. 3(i) indicate that both the A and B beams scan ellipses and not circles on the mDBMC surface due to imperfect alignment of the beam exiting the GRIN lens and the motor axis. The linear plus second-order Fourier series fits of the $\theta_A(n_A)$ and $\theta_B(n_B)$ calibration curves are shown in Fig. 3(ii). Second-order Fourier series fits of the scan pattern function $S(\theta)$ and fixed pattern function $F(\theta)$ are shown in Fig. 3(iii) and (iv) respectively. The minimum, maximum, and average separation of the beams are twice the corresponding values of $S(\theta)$ and are equal to 1.40 mm, 1.60 mm, and 1.49 mm respectively. Thus, the A and B beams scan parallel paths to within ± 0.10 mm along the z dimension.

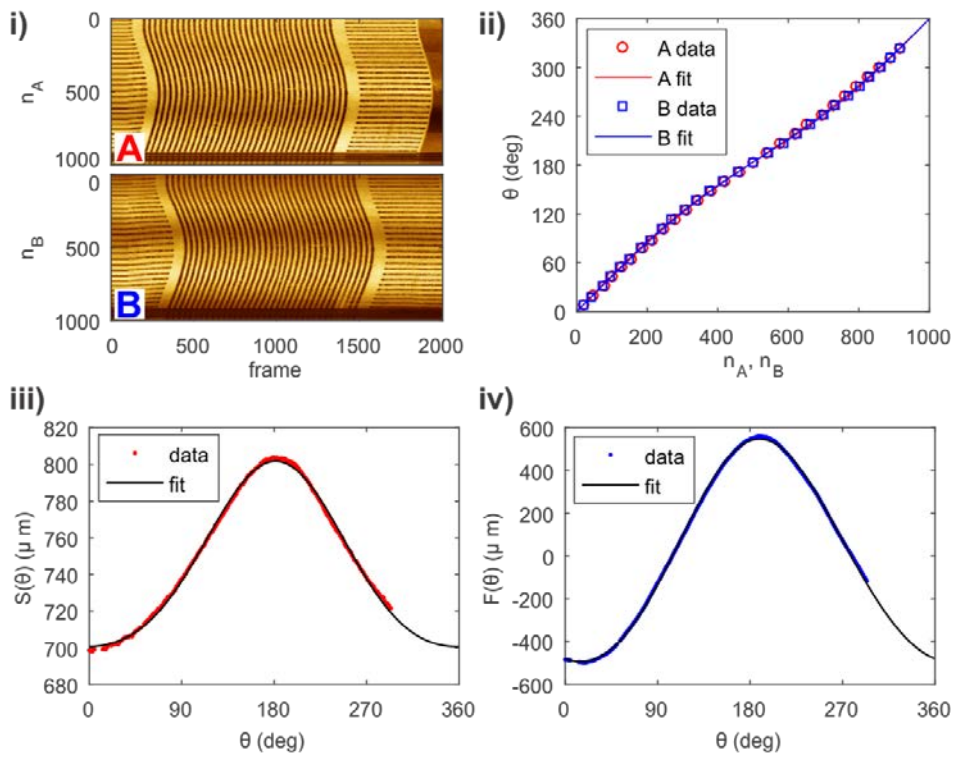

Fig. 3. Calibration of the mDBMC. i) Preprocessed $A(n_A,fr_A)$ and $B(n_B,fr_B)$ images of the calibration pattern. ii) Calibration curves for the conversion of intraframe pixel indices n_A and n_B to θ. iii) Fitted scan pattern function $S(\theta)$. iv) Fitted fixed pattern function $F(\theta)$.

4.2 Printed paper phantom imaging

The preprocessed and θ-calibrated images of the printed QR code phantom are shown in Fig. 4(i). The compression and expansion of the QR code pattern at various points along the fr dimension are indicative of the non-uniform manual actuation velocity along the z dimension

Biomedical Optics EXPRESS

while the wavy appearance of the physically straight paper seam (green arrowheads) shows the manual rotation of the mDBMC during imaging. Horizontal brighter and darker bands, where the θ positions of bright bands in the A image correspond to dark bands in the B image, and vice versa, show the trade-off of light intensities between the A and B beams as the polarization beam splitter rotates. Figure 4(ii) shows the $A^*(fr,\theta)$ and $B^*(fr,\theta)$ images that have been Fourier-filtered along the θ dimension to remove low angular frequencies corresponding to polarization-dependent image intensity variation. The (fr_A,fr_B) and $(fr_A,\Delta\theta)$ maximum intensity projections of the FOXC matrix generated from the $A^*(fr,\theta)$ and $B^*(fr,\theta)$ images are shown in Fig. 4(iii) showing a clear pathway from low frame indices to high frame indices. The (fr_A,fr_B) and $(fr_A,\Delta\theta)$ projections of the points constituting the HCTP are shown as green circles (n = 182) in Fig. 4(iv) while the single point discarded by ensuring that the HCTP consists of the largest ordered triplet set is shown as a red cross. The z and θ velocities and displacements as a function of time derived from the HCTP are shown in Fig. 4(v). The distortion-corrected $A(Z_A,\Theta_A)$ and $B(Z_A,\Theta_A)$ images are shown in Fig. 4(vi). To present the QR code as close as possible to the printed phantom, the heights of the Θ axes in Fig. 4(vi) have been scaled such that they equal the circumference of the 5.0 mm OD plastic tube on which the paper phantom is rolled. As can be seen in Fig. 4(vi), following distortion correction, the seam of the paper phantom has been largely reconstructed as straight and the pixels of the QR code are better aligned and regularly shaped compared to the uncorrected images [Fig. 4(i)].

4.3 Dragon fruit imaging

The preprocessed and θ-calibrated images of the dragon fruit are shown in Fig. 5(i). The black seeds of the fruit are highly scattering and appear as round bright features in the image amongst the fibrous translucent white flesh that appears darker. The dragon fruit seeds are all similar size and shape but the manual actuation of the mDBMC during imaging causes them to appear distorted. As in Fig. 5(i), polarization effects cause the wavy dark/light banding across the images. The Fourier-filtered images $A^*(fr,\theta)$ and $B^*(fr,\theta)$ used for automated frame co-registration are shown in Fig. 5(ii). Figure 5(iii) shows the (fr_A,fr_B) and $(fr_A,\Delta\theta)$ maximum intensity projections of the FOXC matrix. Although less clear than in Fig. 4(iii), a high-correlation pathway is still easily visible from low to high frame indices. The (fr_A,fr_B) and $(fr_A,\Delta\theta)$ projections of the points constituting the HCTP are shown as green circles (n = 74) in Fig. 5(iv). Triplets eliminated from the HCTP due to forced ordering of the triplets to obtain the largest triplet pathway are shown as red crosses (n = 2) while triplets eliminated that would result in unlikely high angular accelerations are shown as red plus signs (n = 2). The estimated z and θ velocities and displacements are shown in Fig. 5(v). In the distortion-corrected images [Fig. 5(vi)], the dragon fruit seeds all appear similar size and shape except for those located at the rightmost edge of the B image. Distortion correction near the edges of images in DMDI is generally worse due to the smaller number of triplets contributing to the velocity estimation in these regions.

5. Discussion

The mDBMC presented in this work retains the advantages of DMDI demonstrated previously with the original DBMC [16]: distortion correction of axial and azimuthal manual actuation, no restrictions on z imaging length, and straightforward one-time calibration. The mDBMC also demonstrates several advantages over the previous DBMC implementation. Most importantly, the automated distortion correction algorithm developed in [17] was successfully adapted to work with the mDBMC beam scanning pattern. This obviates time-consuming and laborious manual image co-registration and increases the potential of endoscopic DMDI technology for clinical use.

Biomedical Optics EXPRESS

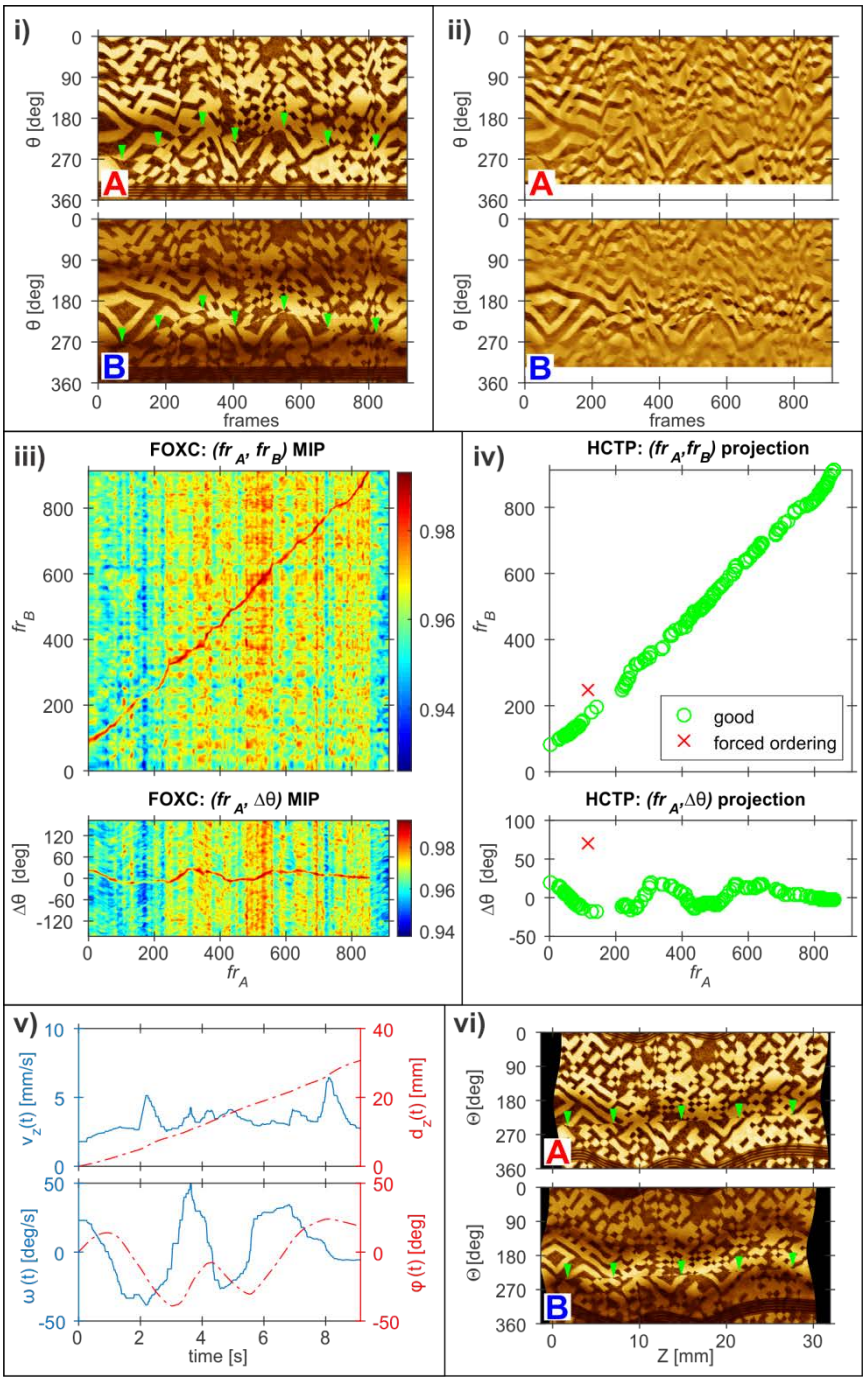

Fig. 4. DMDI imaging of a paper QR code with the mDBMC. i) Preprocessed and θ-calibrated $A(fr,\theta)$ and $B(fr,\theta)$ images. ii) $A^*(fr,\theta)$ and $B^*(fr,\theta)$ images Fourier-filtered along the θ dimension used for frame co-registration. The micromotor cable has been cropped from image. iii) (fr_A,fr_B) (upper) and $(fr_A,\Delta\theta)$ (lower) maximum intensity projections (MIP) of the 3D FOXC (frame-offset cross-correction) matrix. iv) (fr_A,fr_B) (upper) and $(fr_A,\Delta\theta)$ (lower) projections of the HCTP (high correlation triplet pathway) as green circles (n = 182) and triplets filtered as out-of-order as red crosses (n = 1). v) Extracted z and θ velocities and displacements as a function of time. vi) Distortion corrected $A(Z_A,\Theta_A)$ and $B(Z_A,\Theta_A)$ images. Green arrowheads indicate the paper seam in the images.

Biomedical Optics EXPRESS

Unlike the original DBMC, beams from the mDBMC emerge parallel to each other, resulting in higher fidelity for features in the mean intensity projection *en face* A and B images. Additionally, feature co-registration using the three-dimensional OCT data should be more reliable with parallel A and B beams. This property may become more important when co-registering images from samples that have *en face* OCT images that are featureless, feature-sparse, or highly repetitive.

An additional advantage of the mDBMC is that by multiplexing both imaging channels into a single OCT data acquisition channel it requires only half the data bandwidth compared to the original DBMC. This comes at the expense of reduced ranging depth because reflection and scattering far from the mDBMC catheter surface in the A imaging channel appear in the B imaging channel. This imaging channel cross-talk can interfere with feature correlation and reduce the reliability of the automated distortion correction algorithm. A possible solution is to use a laser source with longer coherence length and add a spacer between the polarization beam splitter and cube mirror to create a longer usable ranging depth. However, this solution also increases the average A and B beam separation that concomitantly affects velocity sensitivity. Alternately, rather than using the sheath contours and a fixed distance below them to generate the *en face* A and B images, more advanced image processing methods could be used to segment the A and B channels in the OCT depth dimension by following the sample surface contours.

A potential disadvantage of the mDBMC is that depth multiplexing limits its use to OCT imaging applications. However, additional imaging modalities such as confocal, reflectance, or multiphoton imaging could be added to the mDBMC (for example through the unused fiber of the dual pigtail) that could use the same velocity profiles derived from the OCT channels for distortion correction.

The mDBMC presented in this work is constructed from readily available components and demonstrates proof-in-principle multiplexed DMDI imaging. However, custom optomechanical design could lead to better performance of the mDBMC. For instance, although diagrammed in Fig. 1(ii) as coaxial, the beam exiting the GRIN lens is slightly angled relative to the catheter axis. In addition, the semi-flexible plastic outer tubing of the mDBMC and the FPC folded alongside the motor and optical assembly is cylindrically asymmetric and may not ensure perfect alignment of the axes of the optical subassembly and the micromotor. The non-alignment of the beam exiting the GRIN and the micromotor axis affects imaging in several ways. First, the catheter sheath in Fig. 1(iv) appears at varying distance in the r dimension instead of at constant distance. Thus, producing *en face* images first requires a step to find the contour of the mDBMC sheath. Secondly, the misalignment of the beam and rotational axes results in the non-linear relationship in the $\theta_A(n_A)$ and $\theta_B(n_B)$ calibration plots [Fig. 3(ii)]. This nonlinear transformation adds some complexity and processing time to the distortion correction algorithm as interpolation is needed to generate the calibrated images. Finally, the scan pattern function $S(\theta)$ becomes non-constant and fixed pattern function $F(\theta)$ becomes non-zero when the beam and rotational axes are not aligned. As the automated distortion correction algorithm using frame-to-frame cross correlation assumes a constant separation between the A and B beams, the non-constant $S(\theta)$ function for the mDBMC reduces the ease of finding the HCTP through the FOXC matrix. For a rough comparison, imaging of the QR code using the mDBMC yielded only 182 triplets from 913 image frames (20%) for the HCTP, but for the galvanometer DMDI scanner presented in [17], where $S(\theta)$ is constant to within the optical resolution, the same algorithm yielded 116 triplets from 167 image frames (69%). Similarly for the dragon fruit, the HCTP was 74 triplets from 748 image frames (10%) for the mDBMC, and 130 triplets from 241 image frames (54%) for the galvanometer DMDI scanner. For the dragon fruit, the need for the extra filtering step for generation of the HCTP to remove high angular accelerations is also due to poorer contrast in the FOXC matrix due to non-constant $S(\theta)$. Thus, for these accuracy and processing time considerations, in future realizations of the mDBMC, it would be prudent to develop solutions to align the exit beam of the GRIN with the micromotor axis.

Biomedical Optics EXPRESS

As constructed, the distance between the GRIN lens and micromotor assembly is chosen to give similar but opposite (internal/external) offsets of the working distances of the A and B beams from the catheter surface. This contributes to slight differences in apparent resolutions of the A and B images in Fig. 5(ii) and may affect the reliability of the automated correction algorithm. A more complex optical design with an additional lens element could be used to match the A and B working distances more closely.

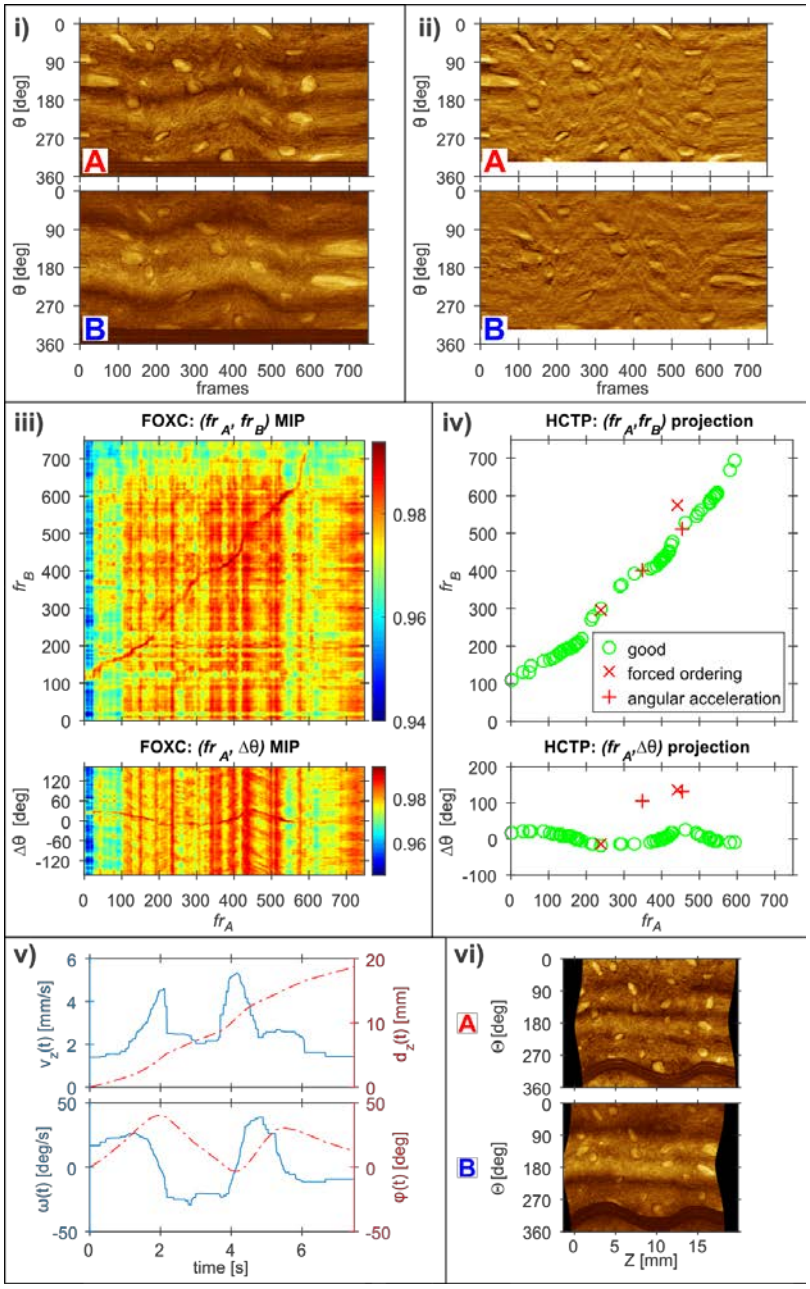

Fig. 5. DMDI imaging of dragon fruit with the mDBMC. Panel arrangement as in Fig. 4 except in iv) the HCTP consists of n = 74 frame-offset triplets (green circles) excluding n = 2 triplets filtered as out-of-order (red crosses) and n = 2 triplets filtered out due to unlikely high angular accelerations (red plus signs).

Biomedical Optics EXPRESS

As with the galvanometer DMDI implementation, the automated distortion correction algorithm is less reliable for high axial or azimuthal accelerations. This is because large differences in the axial helical pitch of the scan patterns, or significant stretching or compression of the image frames in the θ dimension, between the A and B images reduces the magnitude of the frame-to-frame cross-correlation.

A potential challenge with mDBMC imaging is with birefringent samples as, in the absence of catheter rotation, the A and B beams impinge on the sample with orthogonal polarizations. Thus, the A and B images may be too dissimilar to accurately co-register. A possible solution to this problem would be to orient the cube mirror such that the B beam emerges from the catheter at 90° degrees from the A beam in the azimuthal direction. In this way, if the catheter does not rotate while being actuated along the z dimension, the A and B beams hit the part of the sample with the same polarization. An alternate solution for birefringent samples would be to replace the polarization beam splitter with a non-polarizing (50/50) cube beam splitter, which would also have the added benefit of eliminating the need to Fourier filter the initial images to remove polarization effects for the automated distortion correction procedure. However, there would be a 6dB drop in OCT sensitivity corresponding to light from the sample being lost traversing the beam splitter in the return direction. Reflections of the lost light could also potentially interfere with image quality.

The motion distortion correction abilities of DMDI demonstrated thus far are limited to linear motion along the catheter axis, or rotational motion of the catheter, and assume that the sample is rigid. The correction of other motion, such as pitch and yaw of the catheter, or asymmetric distortions of the sample such as deformations of elastic luminal organs, are the subject of further study.

6. Conclusion

We demonstrate a new OCT-specific depth-multiplexed dual-beam micromotor catheter suitable for DMDI. The simple parallel beam scanning pattern allows use of an automated algorithm for generating distortion corrected images. We show successful distortion correction in imaging of a printed paper phantom and a section of dragon fruit.

Funding

Canadian Institutes of Health Research (CIHR) and the National Science and Engineering Research Council of Canada (NSERC).

Acknowledgments

We acknowledge Madeline Harlow and Geoffrey Hohert for helpful discussions and for proofreading the manuscript.

Disclosures

The authors declare that there are no conflicts of interest related to this article.

References

1. D. C. Adams, Y. Wang, L. P. Hariri, and M. J. Suter, “Advances in Endoscopic Optical Coherence Tomography Catheter Designs,” IEEE J. Sel. Top. Quantum Electron. **22**(3), 210–221 (2016).
2. M. J. Gora, M. J. Suter, G. J. Tearney, and X. Li, “Endoscopic optical coherence tomography: technologies and clinical applications [Invited],” Biomed. Opt. Express **8**(5), 2405–2444 (2017).
3. T. Wang, C. Lancée, R. Beurskens, J. Meijer, B. Knapen, A. F. W. van der Steen, and G. van Soest, “Development of a high-speed synchronous micro motor and its application in intravascular imaging,” Sens. Actuators A Phys. **218**, 60–68 (2014).
4. G. J. Ughi, J. Verjans, A. M. Fard, H. Wang, E. Osborn, T. Hara, A. Mauskapf, F. A. Jaffer, and G. J. Tearney, “Dual modality intravascular optical coherence tomography (OCT) and near-infrared fluorescence (NIRF) imaging: a fully automated algorithm for the distance-calibration of NIRF signal intensity for quantitative molecular imaging,” Int. J. Cardiovasc. Imaging **31**(2), 259–268 (2015).

Biomedical Optics EXPRESS

5. D. C. Adler, C. Zhou, T.-H. Tsai, J. Schmitt, Q. Huang, H. Mashimo, and J. G. Fujimoto, "Three-dimensional endomicroscopy of the human colon using optical coherence tomography," Opt. Express **17**(2), 784–796 (2009).
6. M. J. Suter, P. A. Jillella, B. J. Vakoc, E. F. Halpern, M. Mino-Kenudson, G. Y. Lauwers, B. E. Bouma, N. S. Nishioka, and G. J. Tearney, "Image-guided biopsy in the esophagus through comprehensive optical frequency domain imaging and laser marking: a study in living swine," Gastrointest. Endosc. **71**(2), 346–353 (2010).
7. K. Liang, Z. Wang, O. O. Ahsen, H.-C. Lee, B. M. Potsaid, V. Jayaraman, A. Cable, H. Mashimo, X. Li, and J. G. Fujimoto, "Cycloid scanning for wide field optical coherence tomography endomicroscopy and angiography *in vivo*," Optica **5**(1), 36–43 (2018).
8. H. Pahlevaninezhad, A. M. D. Lee, G. Hohert, S. Lam, T. Shaipanich, E.-L. Beaudoin, C. MacAulay, C. Boudoux, and P. Lane, "Endoscopic high-resolution autofluorescence imaging and OCT of pulmonary vascular networks," Opt. Lett. **41**(14), 3209–3212 (2016).
9. D. C. Adams, L. P. Hariri, A. J. Miller, Y. Wang, J. L. Cho, M. Villiger, J. A. Holz, M. V. Szabari, D. L. Hamilos, R. Scott Harris, J. W. Griffith, B. E. Bouma, A. D. Luster, B. D. Medoff, and M. J. Suter, "Birefringence microscopy platform for assessing airway smooth muscle structure and function in vivo," Sci. Transl. Med. **8**(359), 359 (2016).
10. M. J. Gora, J. S. Sauk, R. W. Carruth, K. A. Gallagher, M. J. Suter, N. S. Nishioka, L. E. Kava, M. Rosenberg, B. E. Bouma, and G. J. Tearney, "Tethered capsule endomicroscopy enables less invasive imaging of gastrointestinal tract microstructure," Nat. Med. **19**(2), 238–240 (2013).
11. K. Liang, G. Traverso, H.-C. Lee, O. O. Ahsen, Z. Wang, B. Potsaid, M. Giacomelli, V. Jayaraman, R. Barman, A. Cable, H. Mashimo, R. Langer, and J. G. Fujimoto, "Ultrahigh speed en face OCT capsule for endoscopic imaging," Biomed. Opt. Express **6**(4), 1146–1163 (2015).
12. J. Ren, J. Wu, E. J. McDowell, and C. Yang, "Manual-scanning optical coherence tomography probe based on position tracking," Opt. Lett. **34**(21), 3400–3402 (2009).
13. N. Iftimia, G. Maguluri, E. W. Chang, S. Chang, J. Magill, and W. Brugge, "Hand scanning optical coherence tomography imaging using encoder feedback," Opt. Lett. **39**(24), 6807–6810 (2014).
14. B. Y. Yeo, R. A. McLaughlin, R. W. Kirk, and D. D. Sampson, "Enabling freehand lateral scanning of optical coherence tomography needle probes with a magnetic tracking system," Biomed. Opt. Express **3**(7), 1565–1578 (2012).
15. P. Pande, G. L. Monroy, R. M. Nolan, R. L. Shelton, and S. A. Boppart, "Sensor-Based Technique for Manually Scanned Hand-Held Optical Coherence Tomography Imaging," J. Sens. **2016**, 8154809 (2016).
16. A. M. D. Lee, G. Hohert, P. T. Angkiriwang, C. MacAulay, and P. Lane, "Dual-beam manually-actuated distortion-corrected imaging (DMDI) with micromotor catheters," Opt. Express **25**(18), 22164–22177 (2017).
17. M. Harlow, C. MacAulay, P. Lane, and A. M. D. Lee, "Dual-beam manually actuated distortion-corrected imaging (DMDI): two dimensional scanning with a single-axis galvanometer," Opt. Express **26**(14), 18758–18772 (2018).